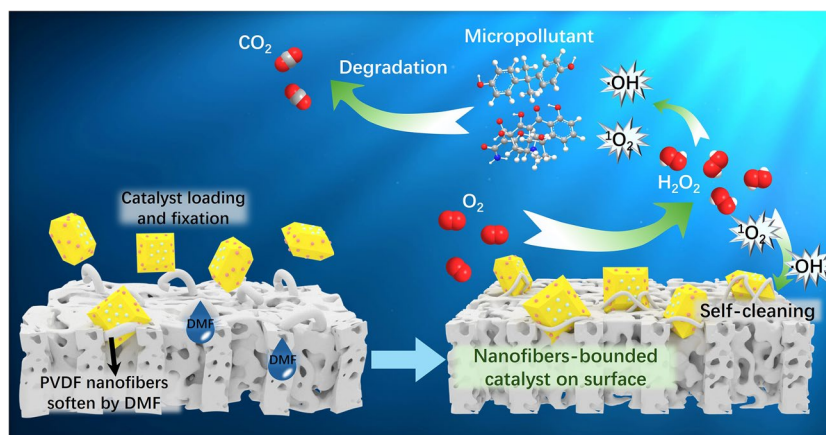**ARTICLE**

Binder-Free Immobilization of Photocatalyst on Membrane Surface for Efficient Photocatalytic H$_2$O$_2$ Production and Water Decontamination

Zhen-Yu Hu[1,2,4], Tian Liu[1,2,3] ✉, Yu-Ru Yang[1,2], Alicia Kyoungjin An[4,5,6] ✉, Kim Meow Liew[2,5,6], Wen-Wei Li[1,2] ✉

HIGHLIGHTS

- Polyvinylidene fluoride nanofibers were treated by dimethylformamide to create micropores on membrane surface.

- Photocatalysts were firmly bounded by nanofibers during stretching and shrinking.

- Particulate catalysts were fixed yet high exposed on the membrane surface.

- Surface self-bounded photocatalytic membrane exhibited tenfold higher decontamination activity than embedded catalyst.

ABSTRACT In photocatalytic water treatment processes, the particulate photocatalysts are typically immobilized on membrane, through either chemical/physical loading onto the surface or directly embedding in the membrane matrix. However, these immobilization strategies inevitably compromise the interfacial mass diffusion and cause activity decline relative to the suspended catalyst. Here, we propose a binder-free surface immobilization strategy for fabrication of high-activity photocatalytic membrane. Through a simple dimethylformamide (DMF) treatment, the nanofibers of polyvinylidene fluoride membrane were softened and stretched, creating enlarged micropores to efficiently capture the photocatalyst. Subsequently, the nanofibers underwent shrinking during DMF evaporation, thus firmly strapping the photocatalyst microparticles on the membrane surface. This surface self-bounded photocatalytic membrane, with firmly bounded yet highly exposed photocatalyst, exhibited 4.2-fold higher efficiency in hydrogen peroxide (H$_2$O$_2$) photosynthesis than the matrix-embedded control, due to improved O$_2$ accessibility and H$_2$O$_2$ diffusion. It even outperformed the suspension photocatalytic system attributed to alleviated H$_2$O$_2$ decomposition at the hydrophobic surface. When

✉ Tian Liu, liutian123@ustc.edu.cn; Alicia Kyoungjin An, alicia.kjan@ust.hk; Wen-Wei Li, wwli@ustc.edu.cn

1 State Key Laboratory of Advanced Environmental Technology, Department of Environmental Science and Engineering, University of Science and Technology of China, Hefei 230026, People's Republic of China

2 SEEM Innovation Center, Suzhou Institute for Advanced Research, University of Science & Technology of China, Suzhou 215123, People's Republic of China

3 School of Resources and Environmental Engineering, Hefei University of Technology, Hefei 230009, People's Republic of China

4 School of Energy and Environmental, City University of Hong Kong, Hong Kong SAR 999077, People's Republic of China

5 Department of Chemical and Biological Engineering, Hong Kong University of Science and Technology, Hong Kong SAR, People's Republic of China

6 Department of Architecture and Civil Engineering, City University of Hong Kong, Hong Kong SAR 999077, People's Republic of China

adopted for UV-based water treatment, the photocatalytic system exhibited tenfold faster micropollutants photodegradation than the catalyst-free control and demonstrated superior robustness for treating contaminated tap water, lake water and secondary wastewater effluent. This immobilization strategy can also be extended to the fabrication of other photocatalytic membranes with diverse catalyst types and membrane substrate. Overall, our work opens a facile avenue for fabrication of high-performance photocatalytic membranes, which may benefit advanced oxidation water purification application and beyond.

KEYWORDS Photocatalytic membrane; Immobilization; Micropollutants; Water treatment; H_2O_2 photosynthesis

1 Introduction

Water pollution by micropollutants, including various endocrine disrupting substances and antibiotics, has raised widespread ecological and health concerns [1–3]. However, low-carbon and economically affordable technologies for efficiently eliminating these micropollutants are still lacking [4]. In this respect, the UV/H_2O_2 advanced oxidation processes hold a great potential, due to less formation of toxic byproduct than the conventional UV/Cl_2 processes for water disinfection and decontamination [5, 6]. In the UV/H_2O_2 process, the H_2O_2 oxidant undergoes photolysis to generate hydroxyl radicals ($\cdot OH$) for pollutant degradation [7, 8]. Therefore, a continuous supply of H_2O_2, either through exogenous addition or through in situ generation, is needed to sustain the reaction [8–10].

Of particular interest is the in situ H_2O_2 generation by electrochemical or photocatalytic processes, which can avoid the complicated processes of H_2O_2 transportation and storage [11–13]. The technologies for H_2O_2 electrosynthesis have been well established to date, but their application niches have been mainly limited to saline wastewater and seawater which feature low ions migration resistance [14–17]. In comparison, H_2O_2 photosynthesis is adaptable to broader range of water matrix due to less restriction by solution conductivity [18–20] and allows for direct integration into UV water treatment process. Nevertheless, the limited activity of the photocatalytic systems presents a significant barrier to their practical environmental application. Especially, the immobilization of particulate photocatalyst onto a membrane substrate, which is typically essential for continuous-flow water treatment, always lead to activity decline [21–24]. In these systems, the catalyst was usually cross-linked to the membrane surface by using binders or was directly incorporated into the membrane matrix during membrane fabrication [25–29]. In either way, the active sites of catalyst were "embedded", limiting their exposure to the bulk water and hence severely restricting

the light penetration and reactant access. For example, the $BiVO_4$ photocatalyst embedded in the polyvinylidene fluoride (PVDF) matrix exhibited only 50% the H_2O_2 photosynthesis activity of the suspended counterpart [30]. Overall, immobilizing the catalyst without compromising the performance remains a key challenge for photocatalytic membrane fabrication and water treatment application.

Here, we propose a binder-free immobilization strategy for stably fixing the catalyst particles on the PVDF surface and meanwhile improving its photocatalytic activity. Previous studies have demonstrated that some chemical agents like dimethylformamide (DMF) can soften or even dissolve PVDF membrane through weakening dipole attraction and hydrogen bond of the PVDF polymer chain [31, 32]. Therefore, we hypothesize that, by fine-regulating the DMF concentration to control the softening degree, the PVDF fibers may be stretched but without causing significant structure damage, thus creating micropores with appropriate pore sizes to hold the particulate catalyst. Then, accompanied with DMF evaporation, the PVDF fibers may undergo shrinking to strap the photocatalyst, thus firmly confining them on the membrane surface without using any chemical binders.

For validation, we adopted a mixed solution of DMF and ethanol for pre-softening the PVDF membrane prior to the photocatalyst loading via vacuum filtration. The faceted $CoO_x/Mo:BiVO_4/Pd$, a particulate inorganic photocatalyst with superior photocatalytic activity and stability for H_2O_2 photosynthesis [33], was adopted for the proof-of-concept study. As expected, the "stretching" and "shrinking" of the membrane fibers during DMF treatment created micropores, with dynamically changed pore sizes, to efficiently confine the photocatalyst microparticles on the membrane surface. In this way, the photocatalysts were firmly bounded yet highly-exposed on the PVDF membrane surface, forming a self-bounded photocatalytic membrane (SSPM). We show that the SSPM was not restricted by light penetration nor

by mass diffusion, thus drastically improving the O_2 accessibility and H_2O_2 diffusion than the conventional matrix-embedded photocatalytic membrane (MEPM). Meanwhile, it far outperformed the membrane with loosely loaded catalyst in terms of operational stability under flow water condition. The SSPM exhibited 4.2 times higher H_2O_2 production rate than the MEPM under simulated solar light and achieved tenfold faster UV photodegradation of tetracycline (TC) and bisphenol A (BPA) than the catalyst-free control. A superior robustness of the UV photocatalytic system for treating real water samples, including tap water, lake water and secondary wastewater effluent, was also demonstrated.

2 Materials and Methods

2.1 Chemicals

The chemicals of K_2CO_3, V_2O_5, $Bi(NO_3)_3 \cdot 5H_2O$, $Co(NO_3)_2$, Na_2PdCl_4, $NaIO_3$, DMF, tetracycline, bisphenol A and $Ti(SO_4)_2$ were purchased from Shanghai Aladdin Biochemical Technology Co., LTD. The PVDF membrane was purchased from Merck & Co., Inc.

2.2 Photocatalyst Preparation

The photocatalysts were prepared following the procedures reported in a previous study [33]. Briefly, single-crystal $BiVO_4$ was prepared by heating the mixture of K_2CO_3 (1.047 g) and V_2O_5 (2.272 g) in a ceramic crucible at a heating rate of 1.5 °C min^{-1} to 450 °C, followed by annealing for 5 h in a muffle furnace. The obtained $K_3V_5O_{14}$ (2 g) was mixed with $Bi(NO_3)_3 \cdot 5H_2O$ (0.326 g) and dispersed in 50 mL water solution under ultrasonication for 30 min. The mixture was then heated at 70 °C for 10 h under ultrasonication, separated by centrifugation, washed with deionized (DI) water, and dried at 70 °C for 8 h.

The as-prepared $BiVO_4$ (0.2 g) was dispersed in 100 mL water, followed by adding 0.1 mol $NaIO_3$ and 0.35 mL $Co(NO_3)_2$ solution (1.5 g L^{-1}). The mixture was purged by N_2 and irradiated for 3 h under a xenon lamp (model 300 DUV; Perfect Light, Inc., light intensity = 0.1 mW cm^{-2}, $\lambda > 420$ nm), filtered, washed with DI water, and dried at 60 °C for 8 h. The as-prepared $CoO_x/BiVO_4$ (0.15 g) was dispersed in 100 mL DI water, followed by addition of 0.182 mL Na_2PdCl_4 solution (3.3 g L^{-1}). The mixture was purged by N_2 and irradiated at $\lambda > 420$ nm for 3 h. As-prepared $CoO_x/BiVO_4/Pd$ was filtered, washed with deionized water, and dried at 60 °C for 8 h.

2.3 Photocatalytic Membrane Preparation

To fabricate the SSPM, a piece of clean PVDF membrane was soaked in the mixed solution of DMF and ethanol (DMF: ethanol = 1: 1 v/v) for 2 min to soften the PVDF fibers. Then, certain amount of catalyst (2 mg unless otherwise specified) was dispersed in 20 mL of the mixed solution (DMF: ethanol = 1: 1 v/v). The suspension solution was filtrated through the above-softened PVDF membrane by vacuum filtration to allow catalyst deposition. Next, the membrane was placed into a fume hood overnight to evaporate the residual DMF and ultimately obtain the SSPM.

For fabrication of the MEPM, the PVDF powder and particulate catalyst were mixed (catalyst: PVDF = 7: 93 w/w) and suspended in the DMF solution. The as-prepared solution was cast on a glass plate using automatic coating machine and casting knife and then immersed in deionized for phase-inversion to form the MEPM. In addition, a surface-unbounded photocatalytic membrane (SUPM), with the catalyst loosely loaded on the membrane surface, was also fabricated by a simple vacuum filtration method. Specific amount of particulate catalysts was suspended in 20 mL ethanol and then filtrated through the PVDF membrane. Then, the membrane was placed in a fume hood overnight to obtain the SUPM. The catalyst loading amount of membrane was calculated based on the catalyst weight and loaded area according to Eq. (1):

$$Loaded\ amount = \frac{catalyst\ weight}{effeective\ loaded\ area\ on\ membrane} \tag{1}$$

2.4 Photocatalytic Experiments

2.4.1 H_2O_2 Photosynthesis Experiment

The H_2O_2 photosynthesis experiment was performed in a beaker, fed with 30 mL DI water and purged with O_2 for 30 min to ensure O_2–saturation. Then, the photocatalytic membrane was immersed in the water solution, and light irradiation was applied to initiate the reaction. A 300-W Xenon

lamp (Beijing Pulinsaisi Technology Co., Ltd.)-equipped filter of AM 1.5G was used as the light source. The light wavelength was from 300 to 1600 nm, and the applied light intensity was 100 mW cm^{-2}. The reaction temperature was controlled at 10 °C. The water samples were collected from the beaker every 20 min during the reaction. For the cyclic experiment, the photocatalytic membrane was cleaned by soaking it in DI water for three times without rinsing, thus avoiding the possible detachment of catalyst from SUPM during non-reaction periods. The H$_2$O$_2$ concentration was measured by titanium sulfate (Ti(SO$_4$)$_2$) colorimetry [34]. Specifically, 0.5 mL sample and 0.5 mL Ti(SO$_4$)$_2$ solution were mixed, and the absorbance at 410 nm was measured by ultraviolet spectrometry.

2.4.2 Micropollutants' Degradation Experiment

The pollutant photodegradation experiment was conducted in a beaker. A low-pressure Hg UV lamp (254 nm wavelength) was used as the light source. The UV fluence was calculated to be 1.08 mW cm^{-2} based on the KI/KIO$_3$ actinometer measurement [35]. TC and BPA, which are ubiquitous in aquatic environment, were selected as model pollutants to evaluate the photocatalytic decontamination performance following the reported procedures [36–38]. Prior to the degradation test, the photocatalytic membrane was immersed 30 mL water solution (containing 5 mg L^{-1} pollutant) and mixed for 15 min in the dark to reach absorption equilibrium. During the photodegradation experiment, the samples were collected regularly for concentration measurement. The TC concentration was measured by a UV spectrometer at 357 nm. The BPA concentration was measured by high-performance liquid chromatography at 273 nm with methanol and pure water mobile phase (70:30 v/v). The formed intermediates during pollutant degradation were detected by UPLC-mass spectrometry (Waters XEVO G2-XS, QTOF) in a negative scan mode of the electron spray ionization source. The mobile phase for BPA measurement was a mixture of acetonitrile/ammonium hydroxide (5 mM) (50:50, v/v), and the mass calibration range was between 50 and 1000 Da with the resolution above 24,000. The mobile phase for TC measurement was a mixture of formic acid solution (0.1%, m/m) and acetonitrile (90:10, v/v), and the mass

calibration range was between 50 and 1000 Da with the resolution above 24,000.

3 Results and Discussion

3.1 Characteristics of the Surface Self-Bounded Photocatalytic Membrane

The SSPM and MEPM, both loaded with faceted CoO$_x$/Mo:BiVO$_4$/Pd as the photocatalyst, were fabricated following the procedures illustrated in Fig. 1a. The composition and structure of the photocatalyst were verified by the X-ray diffraction (XRD) and X-ray photoelectron spectra (XPS) (Figs. S1 and S2). The scanning electron microscopic (SEM) images and energy-dispersive X-ray spectroscopy (EDS) mapping of the SSPM cross-section (Figs. 1b, c and S3a) confirm the deposition of a dense BiVO$_4$ photocatalyst layer on the membrane surface, indicating that they were well retained by the micropores and dispersed on the PVDF surface. A closer observation by high-resolution SEM revealed that the surface-loaded photocatalyst particles were tightly strapped by the PVDF nanofibers, but the catalyst surfaces were sufficiently exposed (Figs. 1d and S3b, c). Notably, the membrane structure of SSPM remained intact, although the membrane shape and internal surface area changed slightly relative to the pristine PVDF membrane (Fig. S4 and Table S1). In contrast, for the MEPM the majority of photocatalysts was embedded within the PVDF matrix rather than on the surface (Fig. 1e-g). Besides, the surface electric potential of SSPM changed from -11.4 to -27.6 mV when raising the pH from 4.0 to 9.0 (Fig. S5a). The surface water contact angle of SSPM was 120.9°, indicating that it had a hydrophobic surface (Fig. S5b).

The SUPM with a loosely loaded photocatalyst on the surface (obtained by vacuum filtration without DMF treatment) was also fabricated for comparison (Fig. S6a). The characterization results confirm that the photocatalyst particles had relatively loose contact with the membrane surface (Fig. S6b), making them vulnerable to detachment under hydraulic water flow condition, as evidenced by the 84.6% loss of catalyst after 30-min crossflow operation with a flow rate of 350 mL min^{-1} (Fig. S7). In comparison, the SSPM exhibited a negligible catalyst loss (~5.4%), confirming its
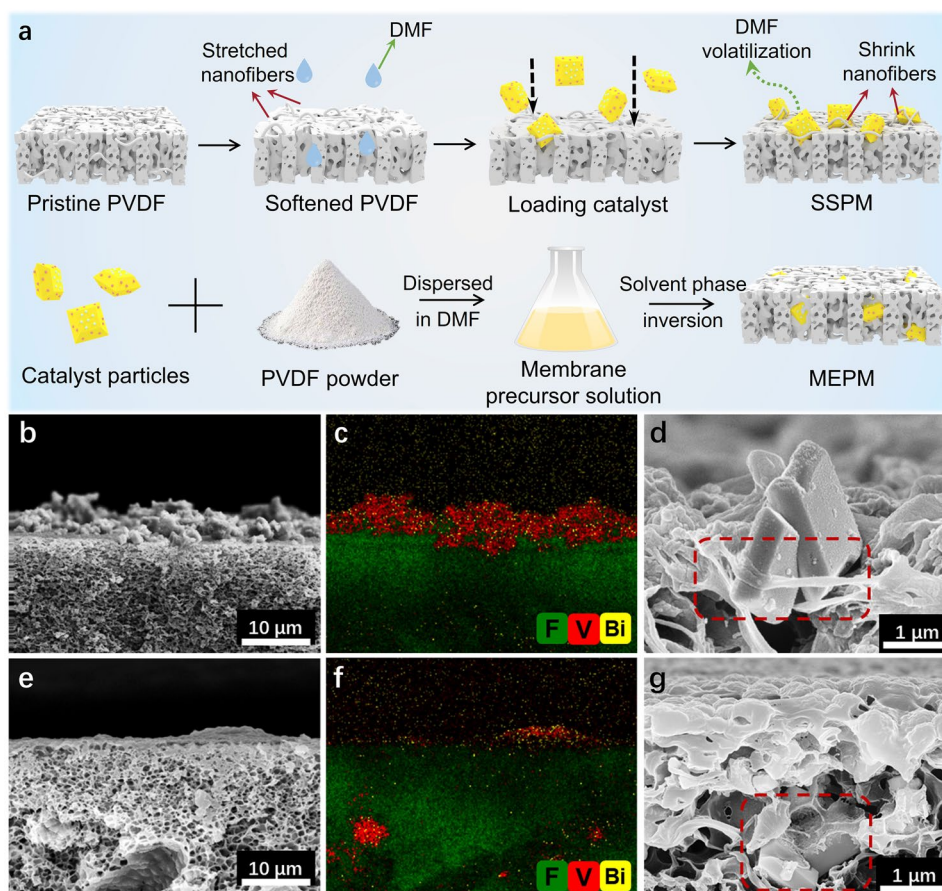
Fig. 1 **a** Procedures for fabrication of SSPM and MEPM; The SEM image, EDS mapping, and high-resolution SEM image of membrane cross-section for **c-e** SSPM and **f–h** MEPM. The red dotted box shows the position of photocatalyst

high mechanical stability. Moreover, the photocatalysts collected from the SSPM exhibited similar morphology and structure to the pristine ones (Fig. S1), indicating that they were physically immobilized without altering the inherent properties. These favorable features rendered the SSPM high efficiency and robustness for continuous-flow water treatment.

3.2 H_2O_2 Photosynthesis Performance of Photocatalytic Membranes

The H_2O_2 photosynthesis activities of the different photocatalytic membranes, all loaded with 1.59 g m^{-2} of photocatalyst, were first evaluated by batch experiment. Here, simulated sunlight was adopted as the light source to facilitate quantification of H_2O_2 production, otherwise under UV-light H_2O_2 photolysis would easily occur. The SSPM

immersed in water exhibited much higher activity than the MEPM for H_2O_2 generation (0.53 vs. 0.12 mM within 2 h) (Fig. 2a). In addition, it also exhibited a higher H_2O_2 production rate (7700 μmol g^{-1} h^{-1}) than the majority of the reported photocatalyst (220~6500) μmol g^{-1} h^{-1} (Fig. 2d and Table S2). Here, the superior photocatalytic activity of the SSPM should be mainly ascribed to the highly exposure degree of its surface-bounded photocatalyst, which favors the light adsorption and easy access of O_2 and H_2O for the photocatalytic reaction (Figs. 2c and S8). In contrast, the slow diffusion of O_2 to the embedded photocatalysts and local accumulation of the generated H_2O_2 severely restricted the MEPM performance.

In addition, the SSPM with firmly bounded catalyst maintained high photocatalytic activity during 20 cyclic runs without obvious performance decline (Figs. 2b and S9), indicating its superior stability during long-time operation.
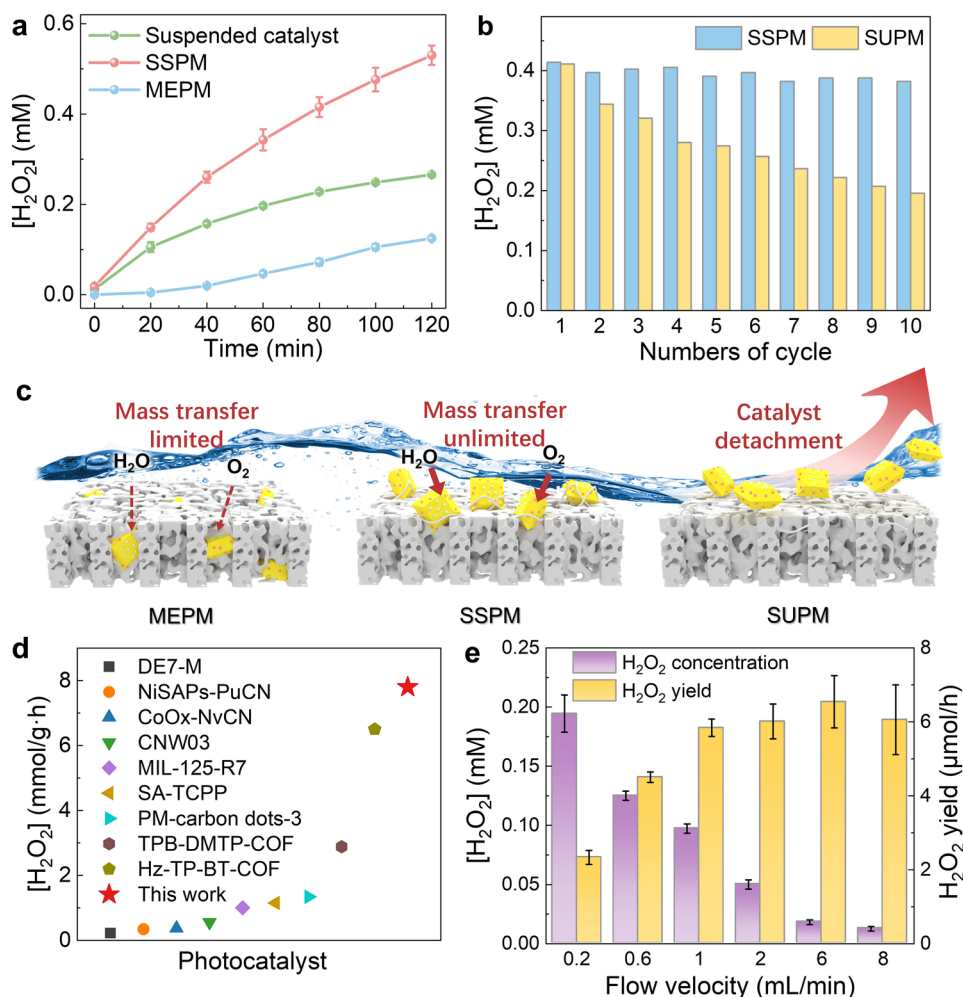
Fig. 2 **a** Photocatalytic H_2O_2 generation by different membranes in a typical batch operation and **b** during 10 operating cycles. **c** Schematic diagram of the membrane under flow-by operation illustrating the different reactant transfer conditions and catalyst stability. **d** Reactivity in comparison with other photocatalysts in the literature. **e** H_2O_2 production during continuous-flow operation with different flow rates.

This is also supported by the SEM image that shows abundant remaining particulate catalyst on the membrane surface after reaction (Fig. S10). In comparison, the SUPM (with loosely immobilized catalyst) exhibited 54.7% activity decay after 10 running cycles, while the membrane-free suspension system (with powder catalyst) exhibited negligible activity after 4 cycles (Fig. S11), possibly due to loss or agglomeration of the suspended particulate catalyst.

To evaluate the potential of the different photocatalyst membranes for practical application, their performances in a membrane cell under continuous-flow operation were also evaluated (Fig. S12). Here, the membrane only served

as a photocatalyst carrier and was operated under flow-by mode: Water flew through the channels above the membrane instead of passing through the membrane matrix since no transmembrane pressure was applied. As expected, the SSPM also stood out as the best one, exhibiting 19-folds higher H_2O_2 production rate than the MEPM (Fig. S13). Notably, the overall H_2O_2 yield of the SSPM could be facilely tuned. The overall H_2O_2 production rate increased from 2.33 to 6.05 µmol h^{-1} when increasing the water flow from 0.2 to 8 mL min^{-1} (Fig. 2e), due to the enhanced interfacial mass transfer under faster flow conditions.

3.3 Reactant Availability and H$_2$O$_2$ Diffusion of Different Membranes

Efficient diffusion of dissolved O$_2$ is critical for the H$_2$O$_2$ photosynthesis in our photocatalytic membrane system (O$_2$ + 2e$^-$ + 2H$^+$ → H$_2$O$_2$) (Fig. S14). The result of Multi-Physics Simulation shows obviously accelerated O$_2$ diffusion and increased O$_2$ accessibility for SSPM than MEPM (Figs. 3a, S15, and S16). The MEPM exhibits a sharp decline in O$_2$ concentration across the PVDF matrix due to the sluggish diffusion rate, thus resulting in severe O$_2$ deficiency for the embedded photocatalysts. In contrast,

higher-concentration O$_2$ was available for the surface-exposed photocatalyst of SSPM, rendering it a high H$_2$O$_2$ production kinetics.

Apart from the improved O$_2$ availability, the improved diffusion and hence less decomposition of the generated H$_2$O$_2$ by SSPM also contributed to its high H$_2$O$_2$ productivity. In the MEPM, the diffusion of H$_2$O$_2$ from the matrix-embedded photocatalyst to the bulk water was restricted; thus, the accumulated H$_2$O$_2$ would undergo rapid decomposition over the photocatalysts (H$_2$O$_2$ + 2 h$^+$ → 2H$^+$ + O$_2$) [39, 40]. In comparison, the generated H$_2$O$_2$ can easily diffuse away from the catalyst on SSPM surface, rendering it even
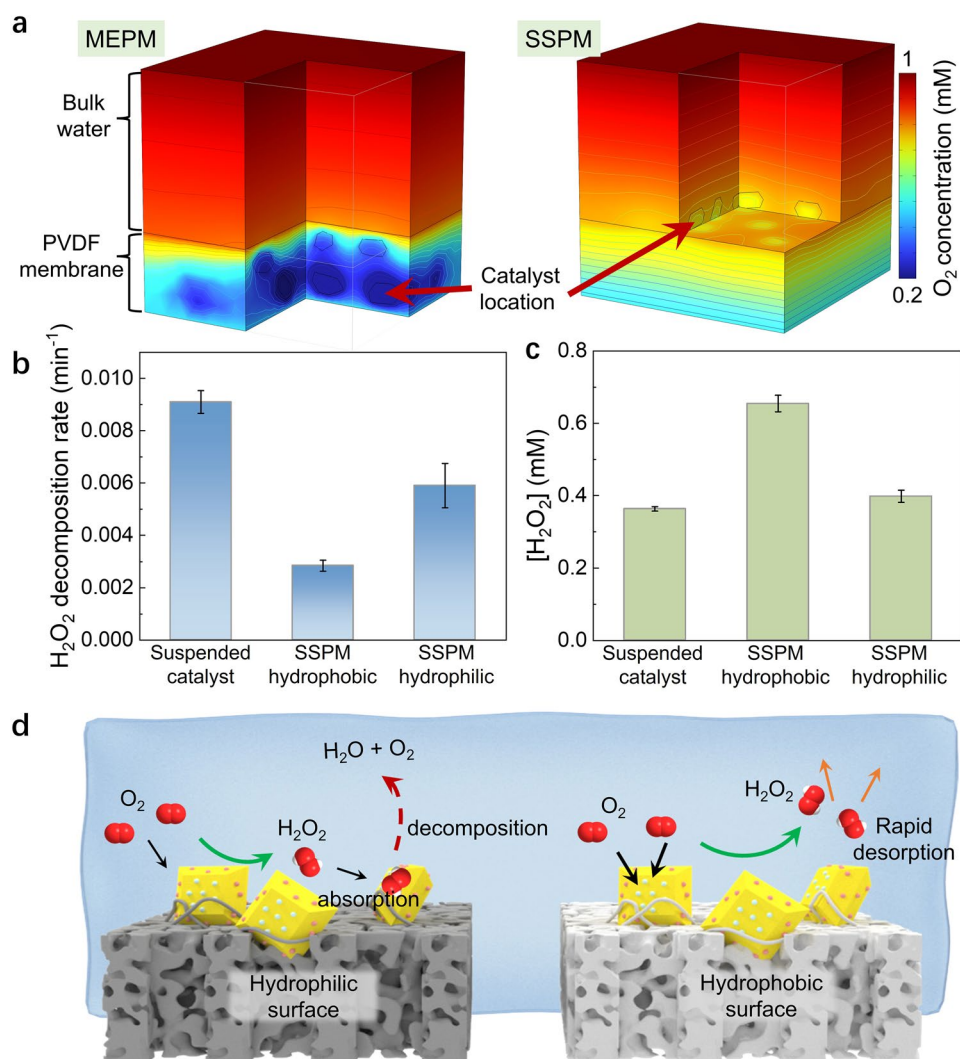

Fig. 3 **a** Modeling result of oxygen distribution in MEPS and SSPM, with bulk O$_2$ concentration of 1 mM and surface oxygen consumption rate of 0.01 mmol s^{-1} (resembling the real reaction condition). **b** H$_2$O$_2$ decomposition rate and **c** accumulative H$_2$O$_2$ production in different photocatalytic systems (Suspended catalyst, SSPM hydrophobic and SSPM hydrophilic). **d** Schematic diagram of H$_2$O$_2$ generation, diffusion and decomposition processes of SSPM with hydrophilic (left) and hydrophobic (right) surface

higher H_2O_2 production rate than in the suspended catalyst system (Fig. 2a) due to increased H_2O_2 desorption/diffusion from the hydrophobic membrane surface [41–43] and hence less H_2O_2 decomposition (Figs. 3b and S17). This was further supported by the fact that shifting from hydrophobic to hydrophilic membrane led to drastically accelerated H_2O_2 decomposition over the catalytic membrane (Fig. S5b). Overall, the efficient reactant diffusion and less H_2O_2 decomposition for the exposed photocatalyst rendered the SSPM superior activity for H_2O_2 photosynthesis (Fig. 3c, d).

3.4 Pollutant Photodegradation Performances and Pathways

The high H_2O_2 photosynthesis activity and stability of the SSPM make it highly adaptable to the widely adopted UV/H_2O_2 processe for water treatment application. We first optimized the photocatalytic performance of the SSPM by batch experiment (Fig. S18). The membrane with optimal catalyst loading of 3.98 g m^{-2} and DMF/ethanol ratio of 1:1 (v/v) was adopted for the subsequent experiments. Impressively, the SSPM achieved complete pollutant removal within 60 min under UV irradiation (Fig. 4a), exhibiting tenfold higher reaction kinetics than that of the UV alone group (Fig. S19). Accordingly, the TOC removal efficiencies were 66.6% and 71.6% for TC and BPA degradation, respectively (Fig. S20). In addition, it exhibited negligible pollutant removal in the dark (Fig. S21), indicating a photodegradation-dominated decontamination process.

The reactive oxygen species (ROS) responsible for pollutant degradation in the UV photocatalytic system was further identified by adding different inhibitors or scavengers: tertiary butanol (TBA) for ·OH, ammonium oxalate (AO) for holes and L-histidine (L-his) for $^1O_2$ (Fig. S22).
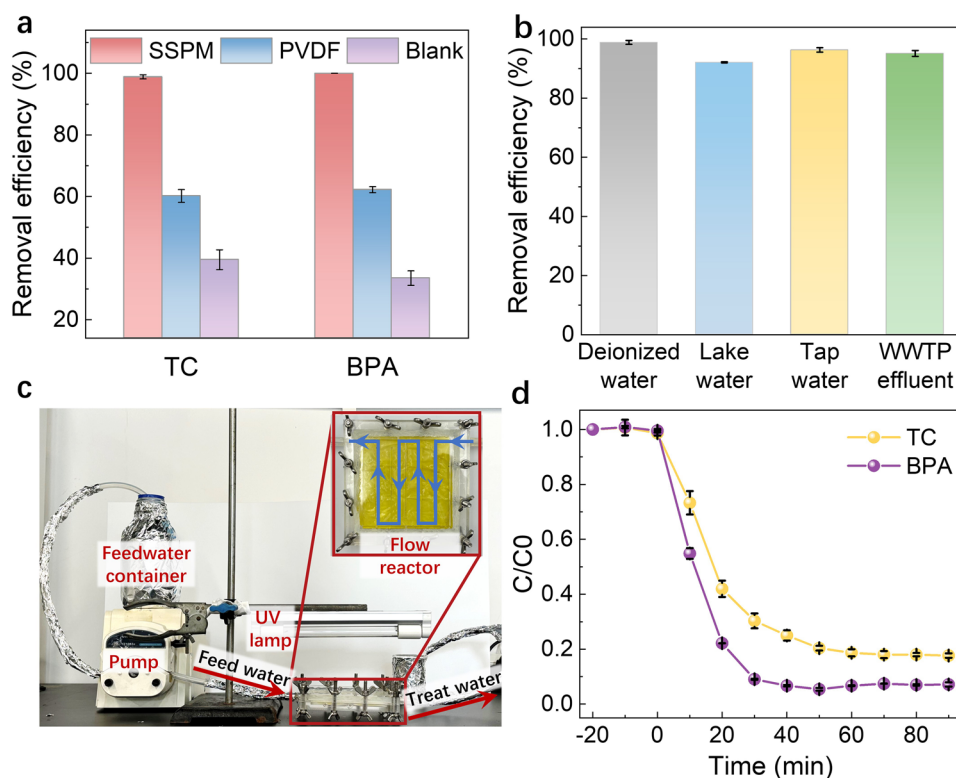

Fig. 4 **a** Pollutant removal ratios of the SSPM under UV light; **b** TC removal ratios of the SSPM for treatment of real water samples; **c** Photograph of experimental setup and **d** pollutant performance of the SSPM-based photocatalytic membrane reactor setup for continuous-flow water treatment. Reaction conditions of batch experiment: pollutant concentration = 10 mg L^{-1}; catalyst loading amount of membrane = 3.98 g m^{-2}; UV fluence = 1.08 mW cm^{-2}, reaction time was 60 min; Reaction conditions of continuous-flow reactor: pollutant concentration = 5 mg L^{-1}; catalyst loading amount of membrane = 3.98 g m^{-2}; UV fluence = 1.08 mW cm^{-2}, the hydraulic retention time was 50 min (flow rate = 0.2 mL min.$^{-1}$)

The markedly inhibited BPA degradation by N_2 purging, which prohibited the generation, confirms a synergistic action between the generated H_2O_2 and UV for augmenting ROS generation and pollutant degradation. Significant suppression was also caused by TBA and L-his, indicating the generation of abundant ·OH and $^1O_2$ in the reaction system. Here, the ·OH should be generated by H_2O_2 photolysis ($H_2O_2 + hv \rightarrow 2\cdot OH$) and $^1O_2$ was generated by the ·OH disproportionation ($4\cdot OH \rightarrow {}^1O_2 + 2H_2O$) [44].

The efficient decomposition of BPA and TC was further validated by liquid chromatograph-mass spectroscopy (LC–MS). According to the values of m/z and chemical structure of intermediate products identified (Fig. S23), the BPA degradation in the photocatalytic system should proceed by two pathways (Fig. S24a). In the first way, the BPA molecule undergoes C–C bond cleavage to form P1, which is further transformed into P2 and P3 through the hydroxylation and oxidization reaction [45]. In the second way, BPA is degraded to P4 and P5 by ·OH attacking; P5 is further transformed into P6 and P7 through dehydroxylation and carbonylation [46], followed by further bond cleavage to form P8, P9 and P10 or mineralization into CO_2 and H_2O. The TC degradation also proceeds by two degradation ways (Fig. S24b). In the first way, TC is attacked by radicals and undergoes demethylation to yield TP1, which further lost the methyl group to form TP2 [47]. In pathway 2, TC undergoes dehydration and N-demethylation to form TP3 and TP4 [48], which is further oxidized into smaller molecules (TP6, TP7, TP8 and TP9) through the cleavage of additional functional groups, intermolecular rearrangement and ring-opening reactions, eventually being mineralized to CO_2 and H_2O.

3.5 Potential for Water Treatment Application

Attributed to the radical–nonradical mixed pathway, the SSPM exhibited superior environmental robustness, remaining over 95% of the degradation activity in the presence of Cl^-, NO_3^- and humic acid, and 80% activity under exposure to SO_4^{2-} and HCO_3^- (Fig. S25). Here, the slight suppression by SO_4^{2-} and HCO_3^- was likely due to SO_4^{2-} competitive absorption on catalyst active site and ·OH scavenging by HCO_3^- [49, 50]. The SSPM also demonstrated superior performance for treatment of real water samples, including lake water, tap water, and secondary effluent from wastewater treatment plant, all achieving > 95% TC removal within 60 min (Fig. 4b).

To facilitate continuous-flow operation for practical water treatment, we further evaluated the SSPM performance under flow-by mode as mentioned above (Fig. 4c). As expected, the system steadily maintained 82% and 93% removal rates for TC and BPA, respectively (Fig. 4d). The superior stability of the SSPM is not only ascribed to the chemical stability of the inorganic catalyst and the PVDF membrane, which are resistant to the oxidative environment (Fig. S26), but also benefited from the unique catalyst immobilization method adopted in this study. In addition, the generated reactive oxygen species can in situ eliminate the membrane foulants (Fig. S27), thus ensuring a long-term stable operation of the SSPM system. All these results suggest that the SSPM could be readily integrated into the UV/H_2O_2 processes to facilitate practical water treatment application.

Apart from catalytic activity, economic cost is also an important consideration for evaluating the application potential of a technology. Therefore, we approximately estimated the fabrication costs (including the materials and energy consumption) of the photocatalytic membranes (detailed in the supplementary information Tables S3-S5). The SSPM and MEPM with different catalyst loadings were fabricated to ensure similar H_2O_2 photosynthesis performances. A comparison of the fabrication cost shows that the SSPM can achieve 39.3% cost saving relative to MEPM (9.948 vs. 16.392 USD m^{-2}) (Fig. S28). Another economic advantage of the SSPM lies in its easy storage in dry state (Fig. S29), in sharp contrast to deactivation of the MEPM after dry storage.

Notably, although we only showcase the construction of SSPM by immobilizing CoO_x/$BiVO_4$/Pd inorganic catalyst on a hydrophobic PVDF membrane, this strategy may be readily extended to other photocatalytic membranes with diverse catalyst types and membrane properties. For example, the particulate catalyst was also successfully self-bounded to the surface of a hydrophilic PVDF membrane, exhibiting similar decontamination performance to that with hydrophobic surface (Fig. S30). This is different from the H_2O_2 photosynthesis process that depends strongly on the membrane surface property, because the generated H_2O_2 was rapidly activated on membrane surface regardless of its hydrophilicity. In addition, the organic photocatalyst of

RF523, a spherical particulate catalyst with diameter of 800 nm, could also be immobilized on PVDF membrane to form a SSPM, achieving tenfold higher H_2O_2 photosynthesis rate than the MEPS (Fig. S31).

Lastly, apart from the crossflow operating mode adopted for the photocatalytic membrane application, the SSPM with hydrophilic surfaces may also be constructed to facilitate flow-through filtration application in the future. In addition, suitable photoreactors should be developed for better integration of the SSPM into the practical UV/H_2O_2 water treatment processes.

4 Conclusion

A unique SSPM was fabricated, and its superior performance for photocatalytic water decontamination was demonstrated. The immobilization strategy adopted here, i.e., chemically softening the PVDF fibers for firmly strapping the photocatalyst particles on the membrane surface, can overcome the challenge of the conventional immobilization approaches that typically compromise the catalytic activity. Benefited from the sufficient exposure of the photocatalysts on membrane surface to improve O_2 accessibility and H_2O_2 diffusion, the SSPM exhibited superior photocatalytic activity, achieving a 4.2-fold higher rate of photosynthesis and tenfold higher kinetics of pollutant degradation than the MEPM under UV irradiation. Our work lays a key basis for advancing photocatalytic technology toward sustainable water purification applications and may offer valuable implications for improved design of various catalytic membranes.

Author Contributions Zhen-yu Hu contributed to conceptualization, methodology, investigation, data analysis, original draft writing and review. Tian Liu contributed to resources, conceptualization, investigation, data analysis and original draft writing. Yu-ru Yang contributed to investigation. Alicia Kyoungjin An contributed to resources, supervision and review. Kim Meow LIEW contributed to resources and supervision. Wen-Wei Li contributed to conceptualization, resources, data analysis, supervision, original draft writing and review.

Declarations

References

1. G. Orive, U. Lertxundi, T. Brodin, P. Manning, Greening the pharmacy. Science **377**(6603), 259–260 (2022). https://doi.org/10.1126/science.abp9554

2. L. Xu, H. Zhang, P. Xiong, Q. Zhu, C. Liao et al., Occurrence, fate, and risk assessment of typical tetracycline antibiotics in the aquatic environment: a review. Sci. Total. Environ. **753**, 141975 (2021). https://doi.org/10.1016/j.scitotenv.2020.141975

3. M.S. Rahman, E.O. Adegoke, M.G. Pang, Drivers of owning more BPA. J. Hazard. Mater. **417**, 126076 (2021). https://doi.org/10.1016/j.jhazmat.2021.126076

4. J. Hu, Y. Lyu, H. Chen, S. Li, W. Sun, Suspect and nontarget screening reveal the underestimated risks of antibiotic transformation products in wastewater treatment plant effluents. Environ. Sci. Technol. **57**(45), 17439–17451 (2023). https://doi.org/10.1021/acs.est.3c05008

5. Y. Zhang, Y.-G. Zhao, F. Maqbool, Y. Hu, Removal of antibiotics pollutants in wastewater by UV-based advanced

oxidation processes: Influence of water matrix components, processes optimization and application: a review. J. Water Process. Eng. **45**, 102496 (2022). https://doi.org/10.1016/j.jwpe.2021.102496

6. R. Wünsch, C. Mayer, J. Plattner, F. Eugster, R. Wülser et al., Micropollutants as internal probe compounds to assess UV fluence and hydroxyl radical exposure in UV/H_2O_2 treatment. Water Res. **195**, 116940 (2021). https://doi.org/10.1016/j.watres.2021.116940

7. Y.-H. Chuang, S. Chen, C.J. Chinn, W.A. Mitch, Comparing the UV/monochloramine and UV/free chlorine advanced oxidation processes (*AOPs*) to the UV/hydrogen peroxide AOP under scenarios relevant to potable reuse. Environ. Sci. Technol. **51**(23), 13859–13868 (2017). https://doi.org/10.1021/acs.est.7b03570

8. H. Li, Z. Wang, J. Geng, R. Song, X. Liu et al., Current advances in UV-based advanced oxidation processes for the abatement of fluoroquinolone antibiotics in wastewater. Chin. Chem. Lett. **36**(4), 110138 (2025). https://doi.org/10.1016/j.cclet.2024.110138

9. Y. Huang, Z. Qiang, Z. Sun, M. Li, Micropollutant degradation by UV/H_2O_2 in drinking water: facilitated prediction through combination of model simulation and portable measurement. Water Res. **221**, 118794 (2022). https://doi.org/10.1016/j.watres.2022.118794

10. Y.-X. Zhang, J.-L. Xiang, J.-J. Wang, H.-S. Du, T.-T. Wang et al., Ultraviolet-based synergistic processes for wastewater disinfection: a review. J. Hazard. Mater. **453**, 131393 (2023). https://doi.org/10.1016/j.jhazmat.2023.131393

11. Q. Zhao, N. Li, C. Liao, L. Tian, J. An et al., The UV/H_2O_2 process based on H_2O_2 *in situ* generation for water disinfection. J. Hazard. Mater. Lett. **2**, 100020 (2021). https://doi.org/10.1016/j.hazl.2021.100020

12. B.C. Kim, E. Jeong, E. Kim, S.W. Hong, Bio-organic–inorganic hybrid photocatalyst, TiO_2 and glucose oxidase composite for enhancing antibacterial performance in aqueous environments. Appl. Catal. B Environ. **242**, 194–201 (2019). https://doi.org/10.1016/j.apcatb.2018.09.102

13. Y. Guo, X. Tong, N. Yang, Photocatalytic and electrocatalytic generation of hydrogen peroxide: principles, catalyst design and performance. Nano-Micro Lett. **15**(1), 77 (2023). https://doi.org/10.1007/s40820-023-01052-2

14. J. Chen, Q. Ma, X. Zheng, Y. Fang, J. Wang et al., Kinetically restrained oxygen reduction to hydrogen peroxide with nearly 100% selectivity. Nat. Commun. **13**(1), 2808 (2022). https://doi.org/10.1038/s41467-022-30411-7

15. X. Yang, Y. Pan, L. Ding, B. Wu, J. Wang et al., Polydopamine/graphite sheet electrode for highly efficient electrocatalytic hydrogen peroxide generation and bisphenol A removal. Chem. Eng. J. **454**, 140026 (2023). https://doi.org/10.1016/j.cej.2022.140026

16. C. Yang, H. Pang, X. Li, X. Zheng, T. Wei et al., Scalable electrocatalytic urea wastewater treatment coupled with hydrogen production by regulating adsorption behavior of urea molecule. Nano-Micro Lett. **17**(1), 159 (2025). https://doi.org/10.1007/s40820-024-01585-0

17. C. Zhao, Z. Ding, K. Zhang, Z. Du, H. Fang et al., Comprehensive chlorine suppression: advances in materials and system technologies for direct seawater electrolysis. Nano-Micro Lett. **17**(1), 113 (2025). https://doi.org/10.1007/s40820-025-01653-z

18. M. Mazzucato, A. Facchin, M. Parnigotto, C. Durante, New and revised aspects of the electrochemical synthesis of hydrogen peroxide: from model electrocatalytic systems to scalable materials. ACS Catal. **14**(9), 6369–6403 (2024). https://doi.org/10.1021/acscatal.4c01011

19. P. Cao, X. Quan, X. Nie, K. Zhao, Y. Liu et al., Metal single-site catalyst design for electrocatalytic production of hydrogen peroxide at industrial-relevant currents. Nat. Commun. **14**(1), 172 (2023). https://doi.org/10.1038/s41467-023-35839-z

20. K. He, Z. Huang, C. Chen, C. Qiu, Y.L. Zhong et al., Exploring the roles of single atom in hydrogen peroxide photosynthesis. Nano-Micro Lett. **16**(1), 23 (2023). https://doi.org/10.1007/s40820-023-01231-1

21. Y. Yang, Y. Li, X. Ma, L. Xie, D. Lv et al., Direct Z-scheme WO_3/covalent organic framework (COF) heterostructure for enhanced photocatalytic hydrogen peroxide production in water. Catal. Sci. Technol. **13**(19), 5599–5609 (2023). https://doi.org/10.1039/d3cy00878a

22. C. Chu, Z. Chen, D. Yao, X. Liu, M. Cai et al., Large-scale continuous and *in situ* photosynthesis of hydrogen peroxide by sulfur-functionalized polymer catalyst for water treatment. Angew. Chem. Int. Ed. **63**(10), e202317214 (2024). https://doi.org/10.1002/anie.202317214

23. M.A. Saflashkar, M. Homayoonfal, F. Davar, Achieving high separation of cephalexin in a photocatalytic membrane reactor: What is the best method for embedding catalyst within the polysulfone membrane structure? Chem. Eng. J. **450**, 138150 (2022). https://doi.org/10.1016/j.cej.2022.138150

24. M. Schröder, K. Kailasam, J. Borgmeyer, M. Neumann, A. Thomas et al., Hydrogen evolution reaction in a large-scale reactor using a carbon nitride photocatalyst under natural sunlight irradiation. Energy Technol. **3**(10), 1014–1017 (2015). https://doi.org/10.1002/ente.201500142

25. C. Chen, L. Fei, B. Wang, J. Xu, B. Li et al., MOF-based photocatalytic membrane for water purification: a review. Small **20**(1), e2305066 (2024). https://doi.org/10.1002/smll.202305066

26. M. Zhang, Y. Yang, X. An, L.-A. Hou, A critical review of g-C_3N_4-based photocatalytic membrane for water purification. Chem. Eng. J. **412**, 128663 (2021). https://doi.org/10.1016/j.cej.2021.128663

27. Y. Shi, J. Huang, G. Zeng, W. Cheng, J. Hu, Photocatalytic membrane in water purification: is it stepping closer to be driven by visible light? J. Membr. Sci. **584**, 364–392 (2019). https://doi.org/10.1016/j.memsci.2019.04.078

28. M.-Y. Yu, J. Wu, G. Yin, F.-Z. Jiao, Z.-Z. Yu et al., Dynamic regulation of hydrogen bonding networks and solvation structures for synergistic solar-thermal desalination of seawater and catalytic degradation of organic pollutants. Nano-Micro Lett. **17**(1), 48 (2024). https://doi.org/10.1007/s40820-024-01544-9

29. Y. Zhang, X. Huang, J. Yeom, A floatable piezo-photocatalytic platform based on semi-embedded ZnO nanowire array for high-performance water decontamination. Nano-Micro Lett. **11**(1), 11 (2019). https://doi.org/10.1007/s40820-019-0241-9

30. X. Zheng, R. Yanagi, Z. Pan, C. Zhou, T. Liu et al., Hydrogen peroxide photosynthesis from water and air using a scaled-up 1–m2 flow reactor. Chem Catal. **5**(3), 101238 (2025). https://doi.org/10.1016/j.checat.2024.101238

31. A. Molliet, S. Doninelli, L. Hong, B. Tran, M. Debas et al., Solvent dependent folding of an amphiphilic polyaramid. J. Am. Chem. Soc. **145**(50), 27830–27837 (2023). https://doi.org/10.1021/jacs.3c11026

32. H. Li, S. Xu, B. Wang, Z. Tian, Z. Xu et al., A new insight into the effects of DMF solvent activation on the polyamide layers of nanofiltration membranes by molecular simulation. J. Membr. Sci. **718**, 123667 (2025). https://doi.org/10.1016/j.memsci.2024.123667

33. T. Liu, Z. Pan, K. Kato, J.J.M. Vequizo, R. Yanagi et al., A general interfacial-energetics-tuning strategy for enhanced artificial photosynthesis. Nat. Commun. **13**(1), 7783 (2022). https://doi.org/10.1038/s41467-022-35502-z

34. M. Jin, Z. Liang, Y. Huang, M. Zhang, H. Fu et al., Boosting enzyme-like activities *via* atomization of cerium for tumor microenvironment-responsive cascade therapy. J. Am. Chem. Soc. **146**(49), 34092–34106 (2024). https://doi.org/10.1021/jacs.4c13573

35. Z. Qiang, W. Li, M. Li, J.R. Bolton, J. Qu, Inspection of feasible calibration conditions for UV radiometer detectors with the KI/KIO$_3$ actinometer. Photochem. Photobiol. **91**(1), 68–73 (2015). https://doi.org/10.1111/php.12356

36. M. Li, F. Liu, Z. Ma, W. Liu, J. Liang et al., Different mechanisms for *E. coli* disinfection and BPA degradation by CeO$_2$-AgI under visible light irradiation. Chem. Eng. J. **371**, 750–758 (2019)

37. X. Qiu, S. Yang, M. Dzakpasu, X. Li, D. Ding et al., Attenuation of BPA degradation by SO4 − in a system of peroxymonosulfate coupled with Mn/Fe MOF-templated catalysts and its synergism with Cl− and bicarbonate. Chem. Eng. J. **372**, 605–615 (2019). https://doi.org/10.1016/j.cej.2019.04.175

38. Y. Liu, S. Liu, M. Chen, Y. Bai, Y. Liu et al., Enhanced TC degradation by persulfate activation with carbon-coated CuFe$_2$O$_4$: The radical and non-radical co-dominant mechanism, DFT calculations and toxicity evaluation. J. Hazard. Mater. **461**, 132417 (2024). https://doi.org/10.1016/j.jhazmat.2023.132417

39. H. Hou, X. Zeng, X. Zhang, Production of hydrogen peroxide by photocatalytic processes. Angew. Chem. Int. Ed. **59**(40), 17356–17376 (2020). https://doi.org/10.1002/anie.201911609

40. M. Sun, X. Wang, Y. Li, H. Pan, M. Murugananthan et al., Bifunctional Pd-O$_x$ center at the liquid–solid–gas triphase interface for H$_2$O$_2$ photosynthesis. ACS Catal. **12**(4), 2138–2149 (2022). https://doi.org/10.1021/acscatal.1c05324

41. Y. Li, Z. Pei, D. Luan, X.W.D. Lou, Triple-phase photocatalytic H$_2$O$_2$ production on a Janus fiber membrane with asymmetric hydrophobicity. J. Am. Chem. Soc. **146**(5), 3343–3351 (2024). https://doi.org/10.1021/jacs.3c12465

42. Y. Chen, L. Zhang, *In-situ* synchronous photoelectrosynthesis of H$_2$O$_2$/HClO green disinfectant with a S-scheme heterojunction bifunctional In$_2$S$_3$/MnIn2S4 photoelectrocatalyst. Appl. Catal. B Environ. Energy **347**, 123768 (2024). https://doi.org/10.1016/j.apcatb.2024.123768

43. L. Cui, M. Sun, Z. Zhang, An efficient, green, and residual oxidant-free wastewater treatment technique enabled by coupling a dual-cathode heterogeneous electro-Fenton process and UV radiation in tandem. Green Chem. **25**(16), 6315–6326 (2023). https://doi.org/10.1039/D3GC01653F

44. Q. Yi, J. Ji, B. Shen, C. Dong, J. Liu et al., Singlet oxygen triggered by superoxide radicals in a molybdenum cocatalytic Fenton reaction with enhanced REDOX activity in the environment. Environ. Sci. Technol. **53**(16), 9725–9733 (2019). https://doi.org/10.1021/acs.est.9b01676

45. S. Gao, C. Guo, J. Lv, Q. Wang, Y. Zhang et al., A novel 3D hollow magnetic Fe$_3$O$_4$/BiOI heterojunction with enhanced photocatalytic performance for bisphenol A degradation. Chem. Eng. J. **307**, 1055–1065 (2017). https://doi.org/10.1016/j.cej.2016.09.032

46. O. Bechambi, S. Sayadi, W. Najjar, Photocatalytic degradation of bisphenol A in the presence of C-doped ZnO: effect of operational parameters and photodegradation mechanism. J. Ind. Eng. Chem. **32**, 201–210 (2015). https://doi.org/10.1016/j.jiec.2015.08.017

47. J. Niu, H.-Z. Lin, S.-G. Jiang, X. Chen, K.-C. Wu et al., Comparison of effect of chitin, chitosan, chitosan oligosaccharide and N-acetyl-d-glucosamine on growth performance, antioxidant defenses and oxidative stress status of *Penaeus monodon*. Aquaculture **372**, 1–8 (2013). https://doi.org/10.1016/j.aquaculture.2012.10.021

48. X. Li, Y. Qiu, Z. Zhu, H. Zhang, D. Yin, Novel recyclable Z-scheme g-C$_3$N$_4$/carbon nanotubes/Bi$_{25}$FeO$_{40}$ heterostructure with enhanced visible-light photocatalytic performance towards tetracycline degradation. Chem. Eng. J. **429**, 132130 (2022). https://doi.org/10.1016/j.cej.2021.132130

49. Y. Liu, H. Liu, C. Wang, H. Sun, L. Wang, An observed "sandwich" framework mediated *via* sulfate ions as electron shuttle for efficient electro-oxidation of organic pollutants. Water Res. **274**, 123139 (2025). https://doi.org/10.1016/j.watres.2025.123139

50. J. Gao, R.F. Nunes, K. O'Shea, G.L. Saylor, L. Bu et al., UV/Sodium percarbonate for bisphenol A treatment in water: Impact of water quality parameters on the formation of reactive radicals. Water Res. **219**, 118457 (2022). https://doi.org/10.1016/j.watres.2022.118457